Supplementary Materials for: A quantitative systems approach to identify paracrine mechanisms that locally suppress immune response to Interleukin-12 in the B16 melanoma model

Yogesh M. Kulkarni,[a] Emily Chambers,[b] A. J. Robert McGray,[c] Jason S. Ware,[a] Jonathan L. Bramson,[c] David J. Klinke II,[a,b,*]

[a]Department of Chemical Engineering and Mary Babb Randolph Cancer Center
West Virginia University (WVU), P.O. Box 6102, Morgantown, WV 26506, USA
[b]Department of Immunology, Microbiology, and Cell Biology, WVU
[c]Department of Pathology and Molecular Medicine, McMaster University,
1200 Main Street West, Hamilton, Ontario, L8N 3Z5, CANADA

[*]To whom correspondence should be addressed. E-mail: david.klinke@mail.wvu.edu

May 28, 2012

This PDF file includes:

Electronic Supplementary Material (ESI) for Integrative Biology

1 Models and Inference

Model-based inference was used to determine the significance associated with dynamic changes in the behavior of the observed system. Here we used models to interpret dynamic changes in cell viability in 2D6 cells upon in vitro culture, in the concentration of IL-12 in the conditioned media, in changes in STAT4 activity in response to rmWISP-1, in the size of B16F10-derived tumors in vivo, and in WISP-1 expression within samples obtained from homogenized B16F10-derived in vivo tumors. In the following sections, we describe these models and the methods for model-based inference.

1.1 Cell Viability Model

The cell viability model was used to describe the changes in cell viability within the experimental system (i.e., an individual well of a 96-well plate) as a function of time. Within this closed system, we assume that live cells have a normally distributed lifespan. The cumulative probability of a cell surviving a defined period of time can then be estimated by:

$$CP = 0.5 \cdot Max \cdot \left[1 - erf\left(\frac{(t - t_s)}{\sigma \cdot \sqrt{(2)}}\right)\right], \tag{1}$$

where CP is the cell viability at time t in percent, Max is the maximum observed cell viability in percent, $erf()$ is the error function, t_s is the average cell lifespan in hours, and σ is the standard deviation in cell lifespan in hours. Values for Max, t_s, and σ are shown in Table S1. Maximum expectation values and 95% confidence intervals were estimated from the experimental data using an empirical Bayesian approach [1]. A Gelman-Rubin multivariate potential scale reduction factor (PSRF) was used to estimate the convergence of the model parameters from three independent chains. For all instances, the multivariate PSRF was below 1.2. For each of the model parameters, the trace of the chains and posterior distribution in the parameters are shown in Figure S4.

1.2 IL-12 Sink Model

A cytokine sink is formed when the catabolism of a cytokine occurs at a rate faster than the cytokine can be replenished. As biological response is dependent on the cytokine concentration within the local cellular microenvironment, the response of neighboring cells to the cytokine can be diminished. Within a stagnant fluid, the local concentration reflects a competition between reaction or catabolism that reduces the local concentration and bulk diffusion that restores local concentrations. In analyzing more traditional reactive systems, dimensionless criteria have been developed to estimate the relative importance of reaction versus diffusion in controlling system behavior. For instance, the Mears Criterion, defined as:

$$\frac{\text{Reaction Rate}}{\text{Diffusion Rate}} < 0.15, \tag{2}$$

is used to determine when external mass transfer effects can be neglected (i.e., diffusion is not rate limiting) [3]. While the reaction rate can be observed directly (in pM per second), the diffusion rate can be estimated by the ratio:

$$\text{Diffusion Rate} = \frac{D_{AB} \cdot C_A}{R^2}, \tag{3}$$

where D_{AB} is the bulk diffusion coefficient of species A in species B, C_A is the bulk concentration of A, and R is the appropriate length scale. Here we used the Mears Criterion to estimate whether the observed catabolism of IL-12 within the system influences the cellular response to IL-12, as the bulk concentration of IL-12 during the experiment is a saturating concentration. For this in vitro system, D_{AB} is estimated to be 500 $\mu m^2/sec$ [6], C_A is the bulk concentration of IL-12 observed using cytometric bead array, and a cell radius was used as the appropriate length scale. The concentration of IL-12 used in calculating the Mears Criterion was the minimum value observed at 30 hours (50 pM). The diameter of T cell was estimated to be 5 μm. In the following paragraph, we describe how we estimated the Reaction Rate from the observed data.

A model was used to describe the changes in concentration of IL-12 within the experimental system as a function of time (i.e., the Reaction Rate) that could be attributed to a cytokine sink. Within this closed system, we assume that change in IL-12 concentration is due to two possible mechanisms: receptor-mediated degradation (R_{RMD}) and a first-order concentration dependent degradation (R_{CDD}). The kinetics for receptor-mediated degradation was expressed in terms of a sigmoidal function:

$$R_{RMD} = \frac{V_{MAX} \cdot C_{IL12}}{K_D + C_{IL12}}, \tag{4}$$

where V_{MAX} is the maximum IL-12 degradation rate when the receptors are saturated, C_{IL12} is the concentration of IL-12, and K_D is the dissociation constant of IL-12 for the receptor. As the high content assay was designed to have saturating concentrations of IL-12 (i.e., $C_{IL12} >> K_D$), the receptor-mediated degradation rate can be approximated as $R_{RMD} = V_{MAX}$. The kinetics for a first-order concentration dependent degradation was expressed as:

$$R_{CDD} = k_{CDD} \cdot C_{IL12}, \tag{5}$$

where k_{CDD} is the degradation rate constant. Collectively, the net rate of change in the concentration of IL-12 within the experimental system was expressed as:

$$\frac{dC_{IL12}}{dt} = -k_{CDD} \cdot C_{IL12} - V_{MAX} \tag{6}$$

The model equations were encoded and evaluated in MatLab V7.0 (The MathWorks, Natick, MA). Summed squared error between experimental and simulated IL-12 concentration measurements was used to determine the likelihood of the model (i.e., $p(Y|\theta, M)$). Posterior distributions in the model predictions (Figure S6) were determined using an empirical Bayesian approach [1], as described in the Model Parameters section. A value of 10^{-3} pM/sec was used as the reaction rate in calculating the Mears Criterion. Using the posterior distribution in the initial reaction rate, this value is an upper limit for both of the experimental conditions (i.e., greater than 95% of the posterior distribution is below this value). Collectively, the values used in calculating the Mears Criterion provide a conservative estimate of the cytokine sink influence within the in vitro assay.

1.3 B16F10 Tumor Growth Model

As illustrated by Figure 6A, the C57Bl/6 mice formed a tumor mass following an intradermal challenge with 10^5 B16F10 cells. The tumor volume was measured using calipers every other day and prior to excision. At day 5, the tumor mass was palpable but was difficult to quantify using calipers. Using the other time points, we used model-based inference to estimate the tumor volume at day 5. A tumor growth model was used to describe the change in the tumor volume (i.e., the number of cells within the tumor mass) as a function of time. In developing the model, we assumed

that tumor cells can choose one of three fates per unit time: remain unaltered, divide, or undergo cell death. As only cell division and cell death alter the number of tumor cells (C_T) within the system, these two cell fates are represented by explicit cellular rates:

$$\frac{dC_T}{dt} = k_p \cdot C_T - k_d(t) \cdot C_T, \tag{7}$$

where $k_p \cdot C_T$ is the rate of cell proliferation and $k_d(t) \cdot C_T$ is the rate of cell death. In the absence of data to support a more complex model, we assume that the rate constant associated with cell proliferation is independent of time while the rate constant associated with cell death is time dependent. The rate constant associated with cell death was estimated at time t using the relationship:

$$k_d(t) = wt_1 \cdot f_G(t, 10) + wt_2 \cdot f_G(t, 12) + wt_3 \cdot f_G(t, 14) + wt_4 \cdot f_G(t, 16) + wt_5 \cdot f_G(t, 18). \tag{8}$$

This function was generated by adding together individual Gaussian functions,

$$f_G(t, t_C) = \exp\left[\frac{-(t - t_C)^2}{2 \cdot (0.625 \cdot 2)^2}\right] \tag{9}$$

that are centered at time t_C (days), normalized to 1 at t_C, and weighted by wt_i. Conceptually, this model is similar to a Malthusian model for population growth with a time-dependent rate parameter. The model equations were encoded and evaluated in MatLab V7.0 (The MathWorks, Natick, MA). Summed squared error between experimental and simulated tumor volume measurements was used to determine goodness-of-fit. Maximum expectation estimates for the calibrated parameters, shown in Table S2, were determined using an empirical Bayesian approach [1], as described in the Model Parameters section.

1.4 Parameters for the IL-12 Sink Model and the Tumor Growth Model

An empirical Bayesian approach was used to estimate the uncertainty associated with the model predictions and model parameters given the available experimental data [1]. Briefly, we used an Adaptive Markov Chain Monte Carlo (AMCMC) algorithm to generate a sequence of states that represent samples drawn from the posterior distribution of the model predictions, given the uncertainty in the model parameters and the specific calibration data. A starting point in the parameter space was obtained via simulated annealing [2]. Using an unbiased prior distribution, a learning period of 100,000 steps was used to establish the covariance of the proposal distribution. The proposed steps within parameter space were evaluated using a Metropolis-Hastings algorithm with a targeted acceptance fraction equal to 0.3. Three parallel chains, each containing 6×10^5 steps, were calibrated to the tumor volume data and used to estimate the posterior distributions in the parameters. The Gelman-Rubin potential scale reduction factor was applied to the model predictions to estimate the convergence of the three Markov chains to the posterior distribution of the model predictions [4, 5], as shown in Figure S9A. For the Tumor Growth Model, an initial sequence of 1.5×10^5 AMCMC steps was required for the three chains to converge. In contrast, the IL-12 Sink Model required a sequence of less than 1.0×10^4 steps to converge. This initial sequence was used as the "burn-in" period. The posterior distribution in the model predictions and model parameters were estimated from the converged segments of the Markov chains (Figure S9B). Using the Tumor Growth Model, the maximum expectation values for the tumor size at day 5 was determined to be 10.4 mm^3 (95% C.I. 4 – 20).

1.5 Quantifying rmWISP-1 inhibition of STAT4 activation

An empirical relationship,

$$pSTAT4 = Max \cdot (1 + \frac{Effect \cdot [WISP1]}{IC50 + [WISP1]}, \tag{10}$$

was used to interpret the dose-dependent inhibition of STAT4 phosphorylation by rmWISP-1. An empirical Bayesian approach was used to estimate the posterior distribution in the model parameters: Max - maximum value of pSTAT4 expressed in terms of mean fluorescent intensity (MFI), $Effect$ - quantifies the dose-dependent effect on pSTAT4 by WISP-1, and $IC50$ - concentration of WISP-1 in ng/ml that exhibits 50% of a maximum effect. The objective of using Similar to the AMCMC approach described in the previous paragraph, three parallel AMCMC chains containing 4×10^5 steps were generated using a learning period of 100,000 steps and a targeted acceptance fraction of 0.4. In contrast to the previous paragraph, the Gelman-Rubin potential scale reduction factor (PSRF) was applied to the model parameters as the relationship, shown in Eqn 10, is a non-linear correlation and does not exhibit a variation in timescales. The traces of the three chains are shown in Figure S10 and the pairwise projections of the posterior distributions in the parameters are shown in Figure S11. The pairwise projects suggest that the parameters can be estimated independently from the observed data. The PSRF applied to the parameters were less than 1.05 for all three parameters, suggestive of convergence. The difference between an experimentally observed variable and the corresponding variable predicted by the model provides an estimate of the variance associated with the assay (i.e., $\epsilon_{Assay} = Y_{Obs} - Y_{Model}$) [8] (see Figure S12). The variance associated with observing the activation state of STAT4 in this assay was empirically estimated and used to identify one outlier in the data set (indicated by $*$ in Figure 5D). This outlier was excluded from subsequent analysis. Note that recombinant proteins may not exhibit the same biological activity as endogenously synthesized proteins. There may be differences in post-translational modifications of the WISP-1 proteins that alter the affinity of protein-protein interactions (see last paragraph in [9]). The data showing that rmWISP-1 dose-dependently inhibits STAT4 have statistical power to establish a one-sided conclusion that WISP-1 causally inhibits STAT4. As increasing concentrations of rmWISP-1 become logarithmically more expensive, the data have limited statistical power to establish the magnitude of STAT4 inhibition, which is a two-sided conclusion.

1.6 In Vitro WISP-1 Expression

To quantify the dynamics of WISP-1 expression by B16F0 cells, we assayed WISP-1 expressed in B16F0-conditioned media at 24 hour intervals (Figure S8C). WISP-1 was quantified by ELISA (DY1627 - R&D Systems, Minneapolis, MN). According to the manufacturers instructions, the ELISA was calibrated over a range of rhWISP-1 concentrations. The data suggest that WISP-1 production by B16F0 cells predominantly occurred within the first 24 hours. We speculate that induction of WISP-1 was a consequence of trypsin-mediated cleavage of E-cadherin. When anchored at the plasma membrane, E-cadherin sequesters beta-catenin [10]. Upon cleavage of E-cadherin, beta-catenin enters the nucleus and induces WISP-1 expression [11]. In vivo, loss of E-cadherin plays an important role in the metastatic potential of cancers [12]. While the in vitro activation of beta-catenin in this system may be artificial, the biological process has clear biological relevance for cancer.

1.7 In Vivo WISP-1 Expression Model

As shown in Figure 6B, expression of mRNA for Wnt-inducible signaling protein-1 exhibits a dependence on tumor size. The metabolic requirements for cell function coupled with the diffusion of nutrients and waste products within the tumor mass results in the stratification of the tumor into different regions: an actively proliferating outer shell, a senescent inner region, and a necrotic core [7]. Based upon the stratification of tumor regions based upon tumor size, we hypothesized three mutually exclusive quantitative hypotheses to explain the dependence of WISP-1 mRNA on tumor size:

1. Hypothesis 1: Cells in inner core express WISP-1.
2. Hypothesis 2: All cells constitutively express WISP-1.
3. Hypothesis 3: Cells in outer shell express WISP-1.

Using a spheroid tumor model, these quantitative hypotheses (i.e., models) were translated into the following mathematical models:

$$\text{Model 1:} \quad C_W = \frac{4}{3}\pi R_i^3 \tag{11}$$

$$\text{Model 2:} \quad C_W = \frac{4}{3}\pi R_o^3 \tag{12}$$

$$\text{Model 3:} \quad C_W = \frac{4}{3}\pi (R_o^3 - R_i^3) \tag{13}$$

$$\text{Total Tumor:} \quad C_T = \frac{4}{3}\pi R_o^3, \tag{14}$$

where C_W is the volume of cells that express WISP-1 mRNA and the radii (R_i, R_o, and ΔR) are defined as in Figure S13. Experimentally, the qRT-PCR measurements of WISP-1 expression were obtained from homogenized B16F10 tumors excised from C57Bl/6 mice and normalized to GAPDH expression. The normalized WISP-1 mRNA expression measurements correspond to

$$\text{Normalized WISP-1 mRNA (nWISP1)} = \frac{a \cdot C_W}{b \cdot C_T}, \tag{15}$$

where a is the level of WISP-1 mRNA in WISP-1 positive cells and b is GAPDH mRNA expression expressed in units of mRNA expression units per cell. The relative WISP-1 mRNA expression for the three competing models can then be expressed as:

$$\text{Model 1:} \quad nWISP1 = \begin{cases} 0 & \text{if } R_o < \Delta R; \\ \alpha \left[1 - 3\frac{\Delta R}{R_o} + 3\left(\frac{\Delta R}{R_o}\right)^2 - \left(\frac{\Delta R}{R_o}\right)^3\right] & \text{if } R_o \geq \Delta R \end{cases} \tag{16}$$

$$\text{Model 2:} \quad nWISP1 = \alpha \tag{17}$$

$$\text{Model 3:} \quad nWISP1 = \begin{cases} \alpha & \text{if } R_o < \Delta R; \\ \alpha \left[3\frac{\Delta R}{R_o} - 3\left(\frac{\Delta R}{R_o}\right)^2 + \left(\frac{\Delta R}{R_o}\right)^3\right] & \text{if } R_o \geq \Delta R \end{cases} \tag{18}$$

where the only independent variable in these models is related to tumor size, R_o. The parameters, ΔR and α, correspond to the thickness of the outer shell and the ratio of cellular expression of WISP-1 mRNA to GAPDH mRNA, respectively.

We are interested in quantifying the relative strength of these models in describing the data, i.e., the conditional probability ($P(M_i|Y)$) of a model (M_i), given the data (Y). While $P(M_i|Y)$ is difficult to estimate directly, Bayes theorem can be used to express this conditional probability in terms of more computationally tractable quantities:

$$P(M_i|Y) \cdot P(Y) = P(Y|M_i) \cdot P(M_i), \tag{19}$$

where $P(Y)$ is the evidence for a model; $P(Y|M_i)$ is the likelihood of observing data Y given model M_i; and $P(M_i)$ is the prior for the model. As we have equal ignorance a priori as to how well the three competing models describe the data, the priors for each model are equal to 1/3. As we are considering three mutually exclusive hypothesis, the evidence for a model can also be expressed as a sum over all of the conditional probabilities:

$$P(Y) = \sum_{i=1}^{3} P(Y|M_i) \cdot P(M_i), \tag{20}$$

such that the evidence for model i is then:

$$P(M_i|Y) = \frac{P(Y|M_i) \cdot P(M_i)}{\sum_{i=1}^{3} P(Y|M_i) \cdot P(M_i)}. \tag{21}$$

As the likelihood, $P(Y|M_i)$, is dependent on the parameter values, we used a Adaptive Markov Chain Monte Carlo (AMCMC) approach, as described in [1], to integrate over the parameter space:

$$P(Y|M_i) = \int_{-\infty}^{\infty} P(Y|\Theta, M_i) \cdot P(\Theta|M_i) d\Theta. \tag{22}$$

The results of the AMCMC integration for all three models are shown in Figure S14. Upon convergence of the chains, the cumulative AMCMC chains represent samples drawn from $P(Y|M_i)$ and can be used to estimate $P(M_i|Y)$, as shown in Figure S15. Using these AMCMC chains, the probability that the evidence favors Model 3 (i.e., $Pr(P(M_3|Y) > 0.95)$) was calculated by kernel density estimation.

2 Proteomics Workflow

2.1 2-D electrophoresis

The resulting pellet from the clean-up of 250 μl concentrated secretome was resuspended in 125 μl of rehydration buffer (7M urea, 2M thiourea, 2% CHAPS, 1% DTT, 2% IPG buffer, 0.002% bromophenol blue) and incubated for 1 h at room temperature prior to rehydration on Immobilized pH Gradient (IPG) strips pH 4-7, 7 cm, (GE Healthcare, Uppsala, Sweden) for 12 h at 25^{o}C. Isoelectric focusing was done using Ettan IPGphor apparatus (Amersham Biosciences) for a total of 18 kVh at 50 μA per strip at 20^{o}C in the following steps: step-n-hold at 300V for 4h, 1000V gradient in 30 min, 5000V gradient in 1h 30 min, followed by step-n-hold at 5000V till 18 kVh was reached. Thereafter, IPG strips were equilibrated in 75mM Tris-HCl pH 8.8, 6M urea, 30% (v/v) glycerol, 2% (w/v) SDS, 0.002% (w/v) bromophenol blue and 1% (w/v) DTT for 30 min. A second equilibration step was done for another 30 min by replacing the DTT with 2.5% iodoacetamide. Equilibrated strips were transferred onto 12% SDS-polyacrylamide gel. IPG strips were sealed with 0.5% (w/v) low melting point agarose in SDS running buffer containing bromophenol blue. Gels

were run at 5mA for 1 h to facilitate a gradual protein transfer from the strip onto the gel, and then at 10mA until the dye front had run off the bottom of the gels. Three biological replicates were obtained for the 0h and 24h secretome each to ensure that the protein expression pattern across each sample was consistent across each replicate. The coomassie stained gels were scanned using Typhoon 9400 scanner (Amersham Biosciences) at 100 μm resolution at normal sensitivity. Data were saved in .gel format using ImageQuant software (Amersham Biosciences). All the protein spots that were well focused were manually excised and digested in-gel using trypsin, as described previously [13].

2.2 MALDI-TOF MS analysis

MALDI-TOF-MS system model Micromass MALDI-R (Waters) was used to obtain the peptide mass fragment spectra as recommended by the manufacturer, as described previously [13]. An external calibration was performed using ProteoMass Peptide MALDI-MS Calibration Kit (Sigma) and provided mass accuracy of 25-50 ppm. Internal calibration was performed with the monoisotopic peaks of Angiotensin II (m/z: 1046.5423), P14R (synthetic peptide) (m/z: 1533.8582) and adrenocorticotropic hormone (ACTH) (18-39) peptide (m/z: 2465.1989). Mass spectral analysis for each sample was based on the average of 800-1000 laser shots. Peptide masses were measured from m/z: 800 to 3,000. The raw spectra was background subtracted, smoothed and deisotoped using ProteinLynxGlobalServer v2.1 (RC5, 2004) using the following parameters - background threshold: 40%, background polynomial: 15, smoothing type: Savitzky-Golay, smoothing iterations: 2, smoothing window: 3 channels, deisotoping type: fast, iterations: 30, threshold: 3%, centroid top: 80%, and minimum peak width: 4 channels. The peak lists containing the m/z ratio and corresponding intensity values were exported to Microsoft Excel for further processing.

2.3 Protein identification using peptide mass fingerprinting

Peptide mass fingerprints obtained from MALDI-TOF MS were used to query public protein primary sequence databases for protein identification. Monoisotopic peaks resulting from internal calibrants were removed before submitting the peak lists to the databases. Mascot database search engine v2.3.02 (www.matrixscience.com, Matrix Science Ltd., UK) and Expasy Aldente (version 19/03/2010) were used to query the UniProtKB/Swiss-Prot mus musculus database (Release 2010-12, 523151 sequences, 184678199 amino acids) with the following settings: peptide mass tolerance of 50 ppm, one missed cleavage site, one fixed modification of carboxymethyl cysteine, one variable modification of methionine oxidation, minimum of four peptide matches and no restrictions on protein molecular mass or isoelectric point. The combined use of two different algorithms offers an advantage of cross validating and consolidating the identification through complementary use of different packages. Aldente, for example, has an added advantage of identifying protein isoforms, a feature that is absent in Mascot. A protein was considered to be positively identified only when it was a hit using both algorithms. Additional criterion for reliable identification was agreement between the theoretical and actual molecular weight and isoelectric point of the protein.

References

1. D. J. Klinke, An empirical bayesian approach for model-based inference of cellular signaling networks. *BMC Bioinform*, 10:371 (2009).

2. K. J. Beers, *Numerical methods for chemical engineering. Applications in Matlab*. Cambridge university Press, Cambridge (2007).

3. H. S. Fogler, *Elements of Chemical Reaction Engineering, 4th ed.*. Prentice Hall Professional Technical Reference, Upper Saddle River, NJ (2006), pg 841.

4. A. Gelman, D.B. Rubin, Inference form iterative simulation using multiple sequences. *Stat Sci*, 7(4):457–474 (1992).

5. S.P. Brooks, A. Gelman, General methods for monitoring convergence of iterative simulations. *J Comput Graph Stat*, 7(4):434–455 (1998).

6. U. Moran, R. Phillips, R. Milo, SnapShot: key numbers in biology. *Cell*, 141:1262.e1 (2010).

7. R. Venkatasubramanian, M.A. Henson, N.S. Forbes, Incorporating energy metabolism into a growth model of multicellular tumor spheroids. *J Theor Bio*, 242:440–453 (2006).

8. D. J. Klinke, I. V. Ustyugova, K. M. Brundage, J. B. Barnett, Modulating temporal control of NF-kappaB activation: Implications for therapeutic and assay selection. *Biophys J*, 94:4249–4259 (2008).

9. L. L. Soon, T. A. Yie, A. Shvarts, A. J. Levine, F. Su, K. M. Tchou-Wong, Overexpression of WISP-1 down-regulated motility and invasion of lung cancer cells through inhibition of Rac activation. *J Biol Chem*, 278:11465–70 (2003).

10. S. Orsulic, O. Huber, H. Aberle, S. Arnold, R. Kemler, E-cadherin binding prevents b-catenin nuclear localization and b-catenin/LEF-1-mediated transactivation. *J Cell Sci*, 112:1237–1245 (1999).

11. L. Xu,1 R. B. Corcoran, J. W. Welsh, D. Pennica, A. J. Levine, WISP-1 is a Wnt-1- and beta-catenin-responsive oncogene. *Genes Dev*, 14:585–595 (2000).

12. T. T. Onder, P. B. Gupta, S. A. Mani, J. Yang, E. S. Lander, R. A. Weinberg, Loss of E-Cadherin Promotes Metastasis via Multiple Downstream Transcriptional Pathways. *Cancer Res*, 68:3645–3653 (2008).

13. Y. M. Kulkarni, V. Suarez, D. J. Klinke, Inferring predominant pathways in cellular models of breast cancer using limited sample proteomic profiling. *BMC Cancer*, 10:291 (2010).

14. I. Airoldi, E. Di Carlo, C Cocco, G Taverniti, T. D'Antuono, E. Ognio, M. Watanabe, D. Ribatti, P. Pistoia, Endogenous IL-12 triggers an antiangiogenic program in melanoma cells. *Proc Natl Acad Sci USA*, 104(10):3996–4001 (2007).

Supplemental Tables

Table S1: **Values for cell viability model parameters.**

Experimental Conditions	Max (%) Median (95% C.I.)	t_s (hours) Median (95% C.I.)	σ (hours) Median (95% C.I.)
2D6 only	66.3 (64.8 - 67.9)	24.1 (19.9 - 30.1)$^{+}$	18.1 (12.9 - 27.0)
2D6 + IL12	66.3 (64.8 - 67.9)	33.0 (31.4 - 35.1)$^{+}$ *	5.8 (3.0 - 8.5)
2D6 + B16F0	58.9 (56.1 - 61.7)	20.7 (18.1 - 23.7)**	5.1 (0.4 - 7.7)
2D6 + B16F0 + IL12	58.9 (56.1 - 61.7)	25.6 (23.9 - 27.2)* **	5.6 (3.6 - 8.5)

* ($p < 0.001$), $^{+}$ ($p < 0.01$), and ** ($p < 0.01$) indicate a significant difference between the cellular lifespans (t_s) for two conditions.

Table S2: **Values for tumor growth model parameters and initial condition.**

Parameter Name	Units	Untreated C56Bl/6
$C_T(t=0)$	mm^3	0.489
k_p	days^{-1}	6.09×10^{-1}
wt_1	days^{-1}	1.14×10^{-4}
wt_2	days^{-1}	7.50×10^{-7}
wt_3	days^{-1}	3.59×10^{-1}
wt_4	days^{-1}	6.83×10^{-3}
wt_5	days^{-1}	3.79×10^{0}

The values for the parameters and initial conditions correspond to the maximum expectation values that were estimated from the converged segments of three independent AMCMC chains.

Table S3: **2x2 Contingency Table for Exosome Functional Annotation.**

	Focus Genes	Non-focus Genes	Row Total
Genes/Proteins associated with exosome	20	1264	1284
Genes/Proteins not associated with exosome	19	23497	23516
Column Totals	39	24761	24800

Supplemental Figures

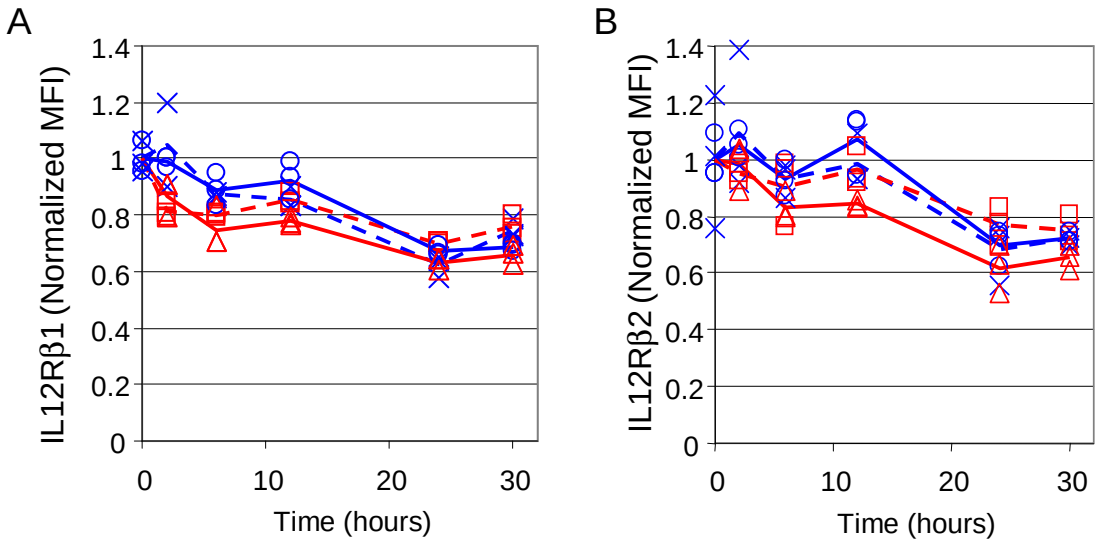

Figure S1: **IL-12 receptor expression in 2D6 cells during high content assay.** Changes in IL12Rβ1 (panel A) and IL12Rβ2 (panel B) were quantified as a function of time by flow cytometry for the four experimental conditions (B16F0 + 2D6 co-culture - dotted lines, x's and squares; 2D6 alone - solid lines, o's and triangles; unstimulated - blue x's and o's; IL12 stimulated - red squares and triangles). The changes in cellular IL12Rβ2 were represented by median values of the unimodal distribution in MFI for CD45$^+$ events (i.e., 2D6 cells). Mean response at each time point and condition were used to create trend lines (solid and dotted lines). Results from three technical replicates are shown and are representative of at least two biological replicates.

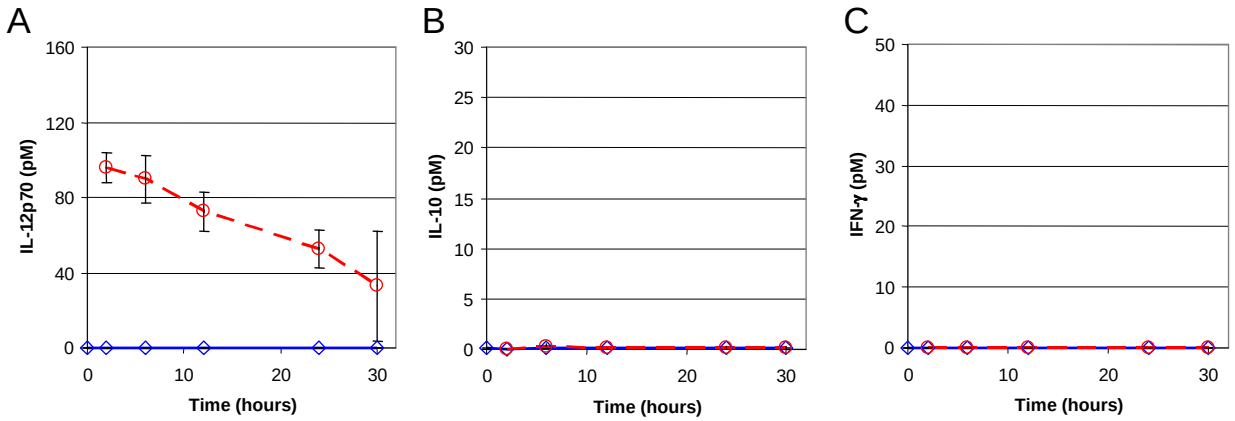

Figure S2: **Cytometric bead array results for B16F0 cells alone.** Changes in IL-12p70 (panel A) and enrichment of IL-10 (panel B) and IFNγ (panel C) in B16F0 conditioned media were quantified as a function of time using cytometric bead array (mean $\pm$ standard deviation). Results are shown for two experimental conditions: B16F0 + IL-12 (red circles and red dotted line) and B16F0 cells alone (blue diamonds and blue solid lines). Results from three technical replicates are shown.

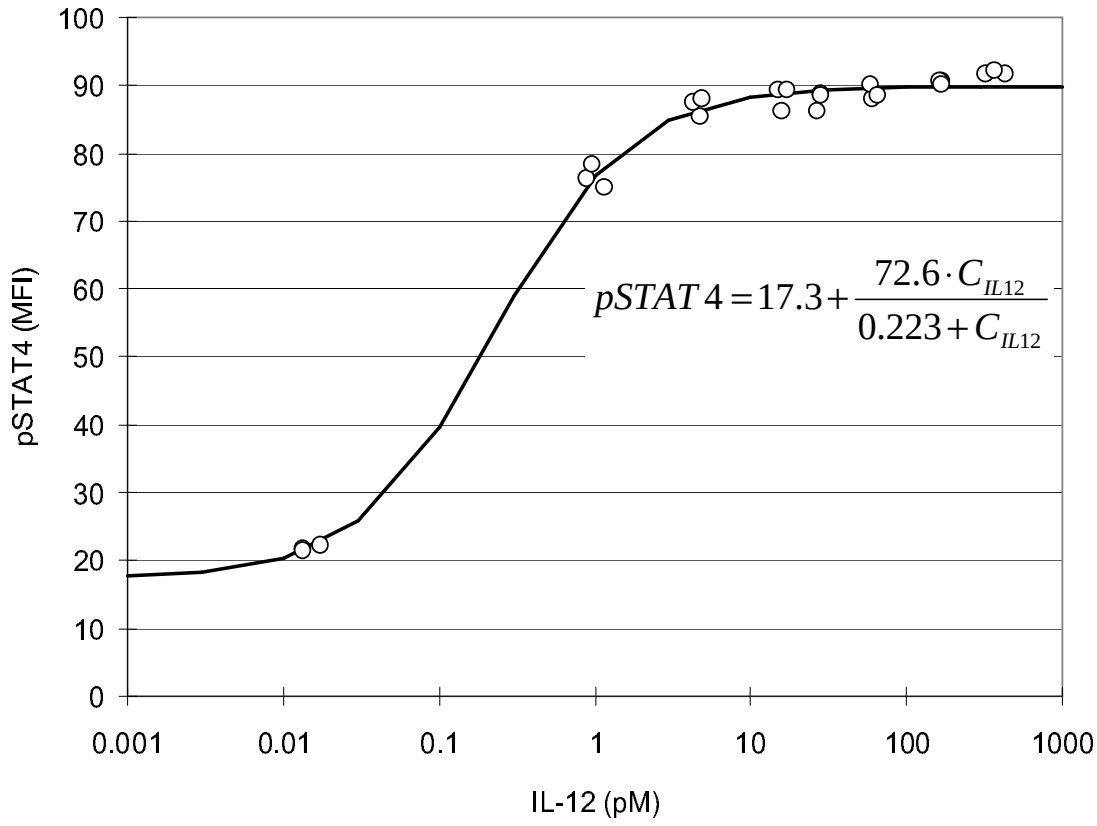

Figure S3: **IL-12 dose-dependent phosphorylation in STAT4 in 2D6 cells.** Following preconditioning in cRPMI for 12 hours, 2D6 cells were stimulated with IL-12 at the indicated dose for 2 hours. Phosphorylation of STAT4 was measured by flow cytometry. The concentration of IL-12 used was also measured using an IL-12p70 BD Cytometric Bead Array. The median results for each replicate are indicated by the circles.

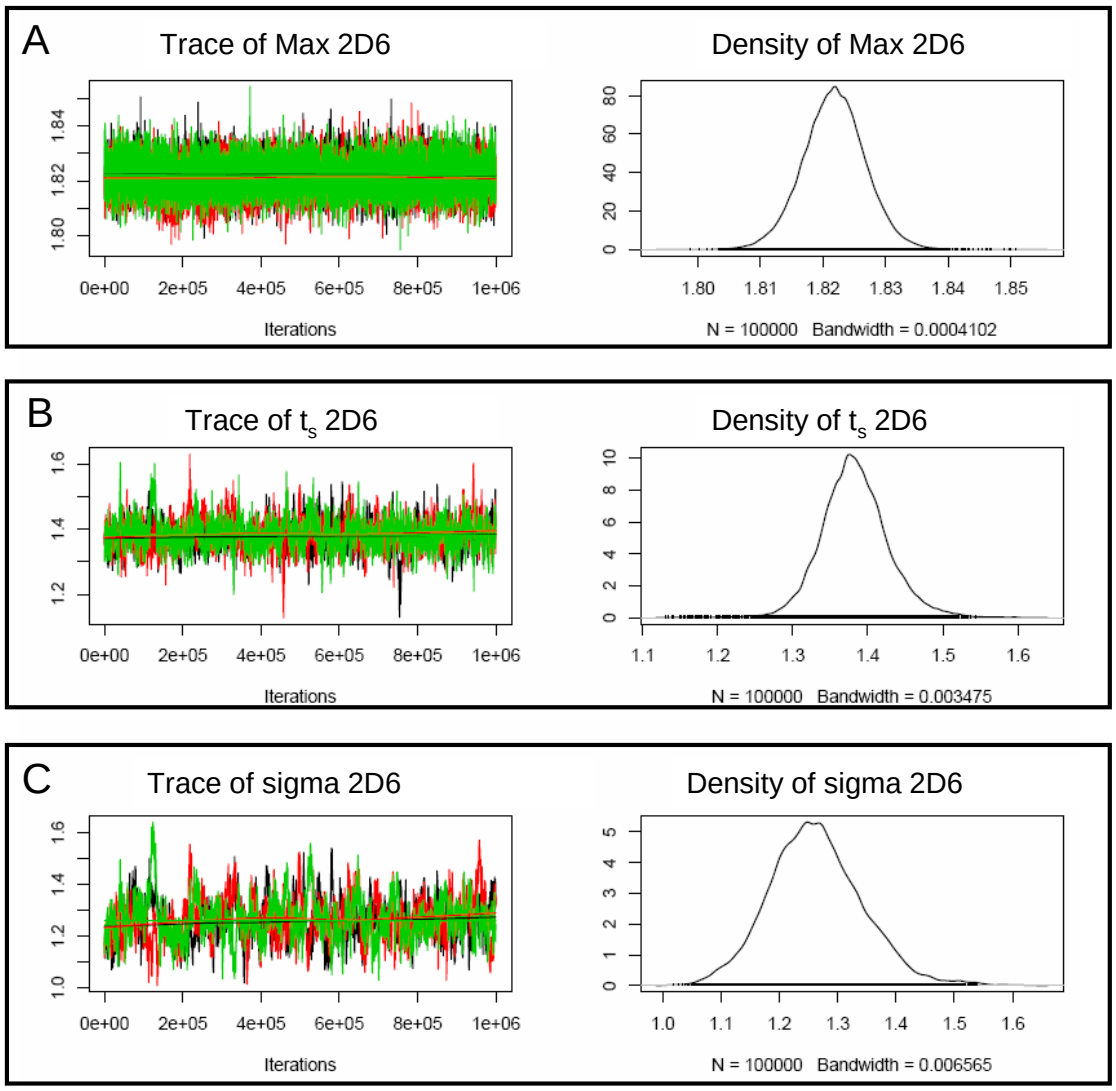

Figure S4: **Trace of and posterior distributions in the cell viability model parameters.** Summary trace plots (left panel) of the $\log_{10}$ of the parameters and cumulative posterior distribution (right panel) are shown for the following conditions: (A) Maximum viability for 2D6 cells, (B) t_s for 2D6 only, (C) σ for 2D6 only, (D) t_s for 2D6 plus IL12, (E) σ for 2D6 plus IL12, (F) Maximum viability for 2D6 plus B16 co-culture, (G) t_s for 2D6 plus B16, (H) σ for 2D6 plus B16, (I) t_s for 2D6 + B16 + IL12, and (J) σ for 2D6 + B16 + IL12. The results from the converged segments of three different Markov chains, with 1×10^6 steps in each chain, are shown in different colors: chain 1 - green, chain 2 - black, and chain 3 - red.

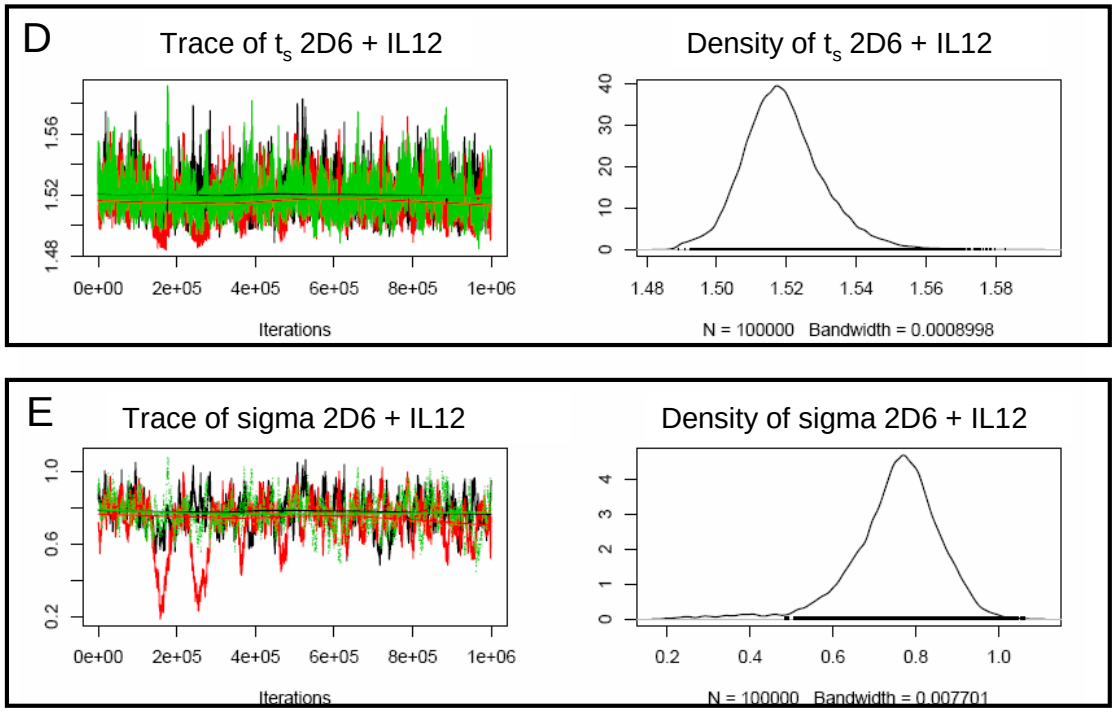

Figure S4 - continued.

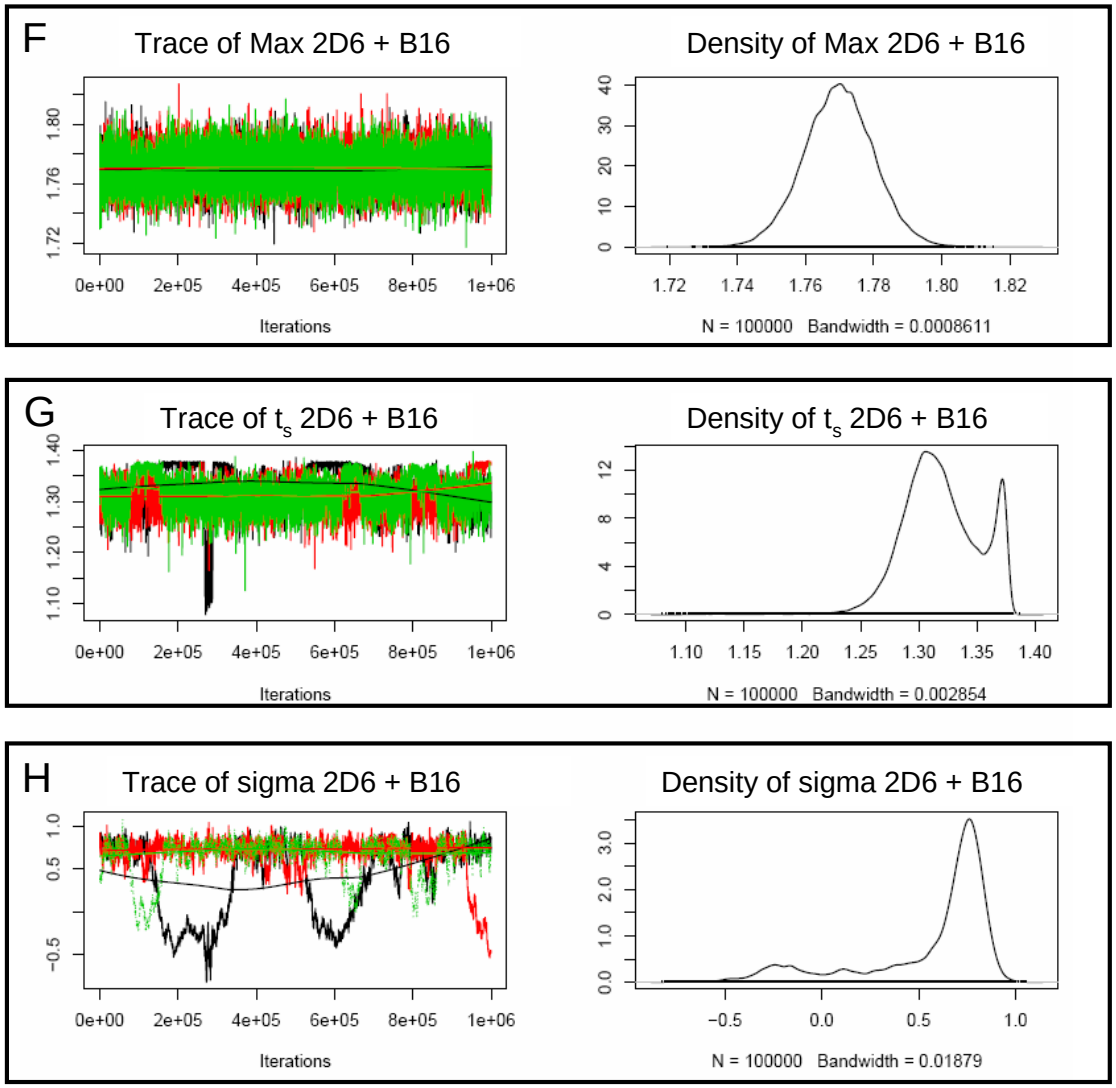

Figure S4 - continued.

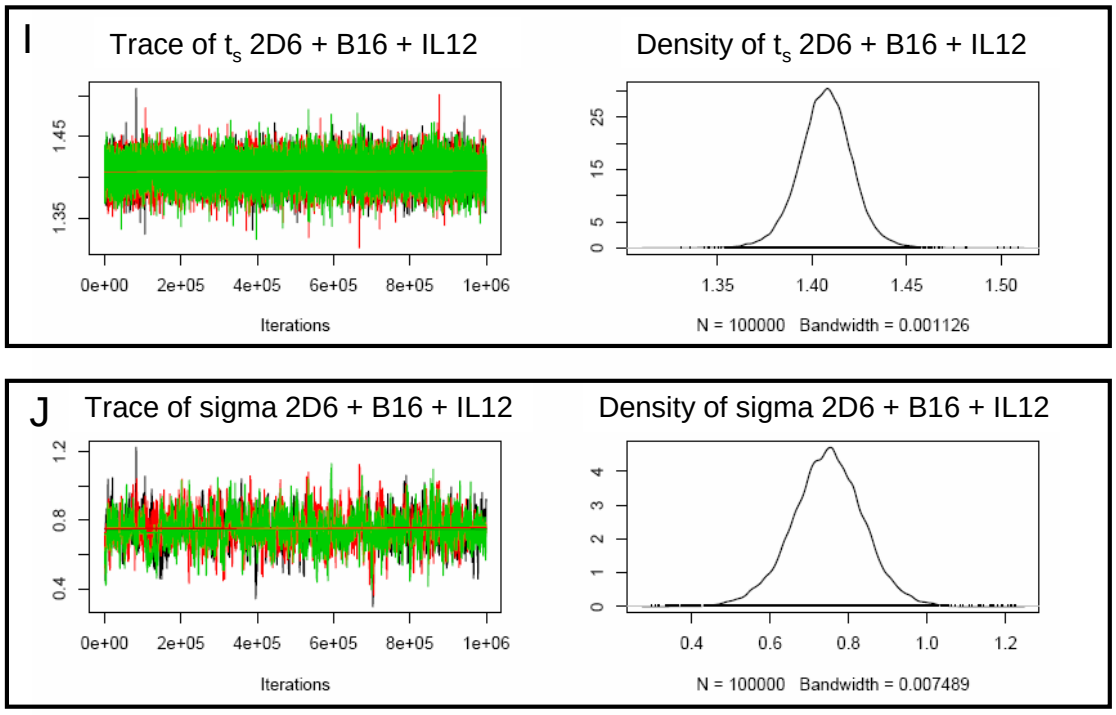

Figure S4 - continued.

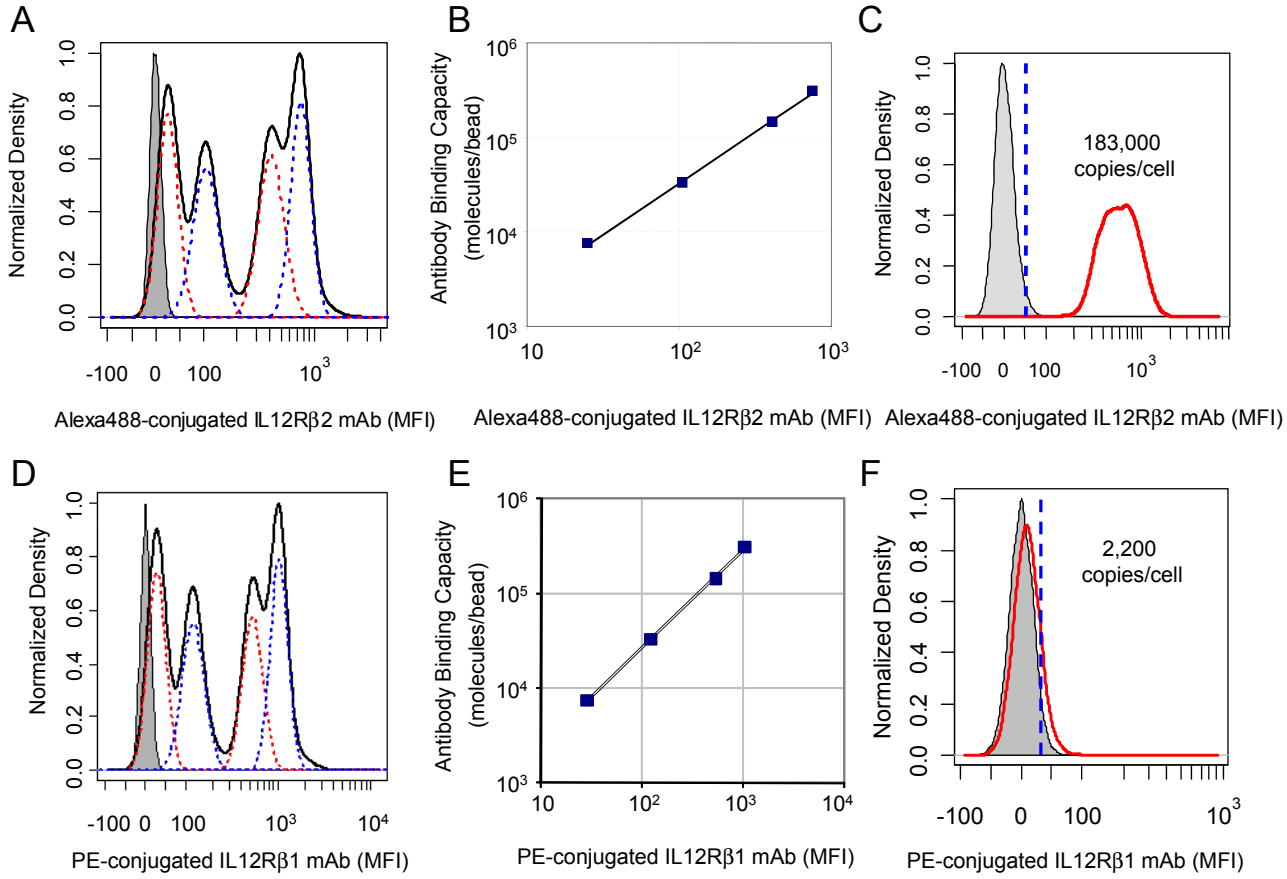

Figure S5: **B16F0 cells express components of the IL-12 receptor.** Assay of IL-12 receptor $\beta 1$ and IL12R$\beta 2$ expression in B16F0 cells by flow cytometry. Copy number expression was obtained using five Quantum Simply Cellular microsphere populations, one blank and four labeled with increasing amounts of anti-mouse IgG antibody, that exhibit a defined antibody binding capacity. Probability density functions for the five microsphere populations stained using Alexa 488-conjugated mouse anti-IL12R$\beta 2$ mAb (Panel A) and using PE-conjugated mouse anti-IL12R$\beta 1$ mAb (Panel D). Plots of the median MFI for the four antibody-stained microspheres versus the corresponding antibody binding capacity, expressed in molecules per bead (IL12R$\beta 2$ - panel B, IL12R$\beta 1$ - panel E). Marginalized probability density functions (PDF) for the mean fluorescent intensity that correspond to IL-12R$\beta 2$ (panel C) and IL-12R$\beta 1$ (panel F) annotated with the corresponding protein copy number. To be conservative in our estimate of cellular copy number, we assumed that the antibody:target ratio was 1:1. Unstained B16F0 cells were used as a negative control (gray shaded curve). The dotted vertical line indicates a data-driven threshold whereby 95% of the unstained cells exhibited a MFI below the threshold. Similar results for IL-12R$\beta 1$ expression was reported previously by Airoldi et al. [14]. Results representative of three replicates.

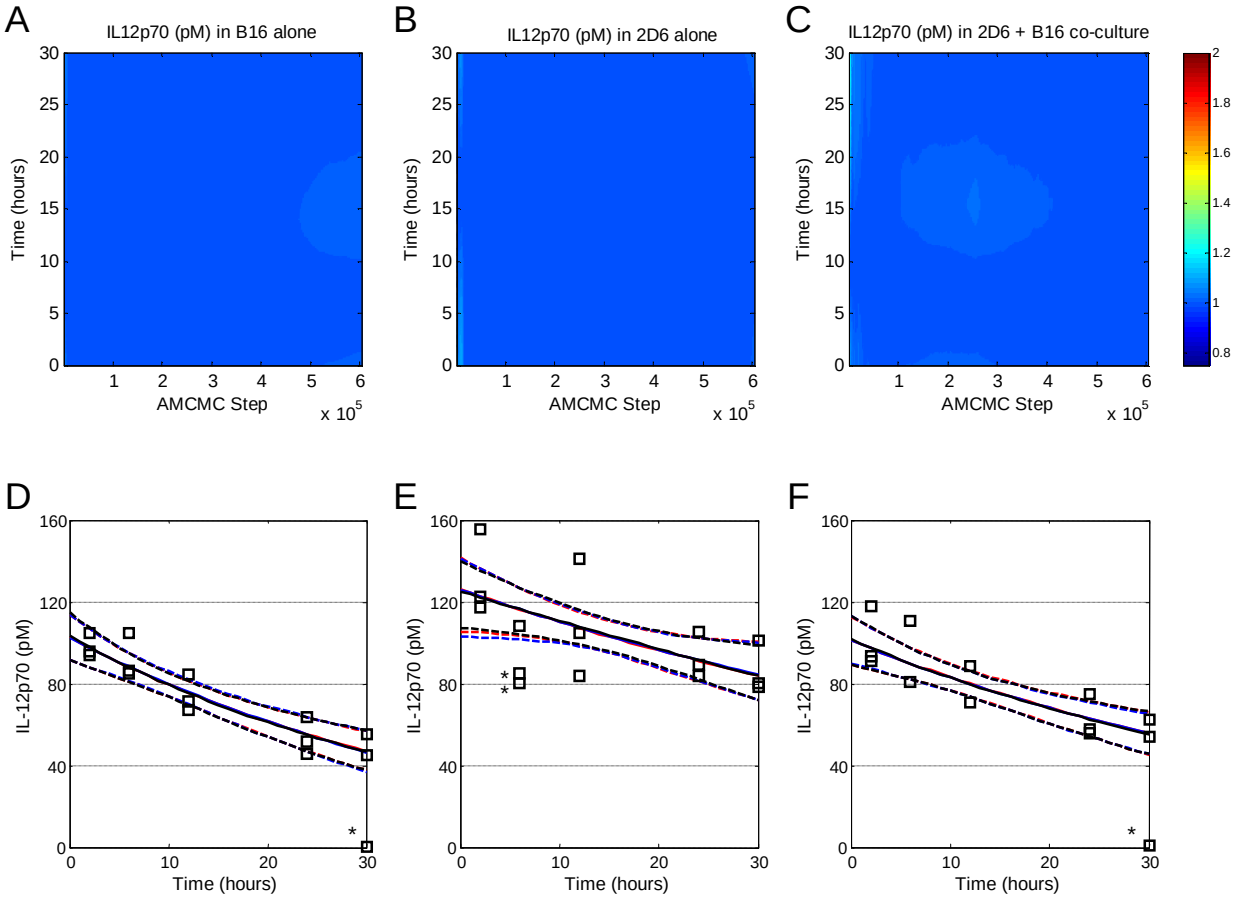

Figure S6: **Convergence of and posterior distributions in the IL-12 Sink Model predictions.** The results for model-based inference are shown for three different experimental conditions: B16 alone (Panels A and D), 2D6 alone (Panels B and E), and 2D6+B16 co-culture (Panels C and F). (Panels A-C) A contour plot of the Gelman-Rubin statistic (i.e., the z-axis equals the potential scale reduction factor) of the model predictions as a function of time (i.e., the y-axis) calculated as a function of the cumulative chain up to a specific AMCMC step (i.e., the x-axis). Three parallel chains were used to calculate the Gelman-Rubin statistics for the model-based inference of the IL-12 cytokine sink. Values less than 1.2 suggest convergence of the chains. (Panels D-F) Comparison of the posterior distribution in the model predictions (lines) with the IL-12 concentration data (squares). The most likely predictions are represented by the solid lines. The dashed lines enclose the 95% confidence intervals. The results from the converged segments of three different Markov chains, with 5.5×10^5 steps in each chain, are shown in different colors: chain 1 - blue, chain 2 - black, and chain 3 - red. Data points highlighted with * were considered outliers and not included in the analysis.

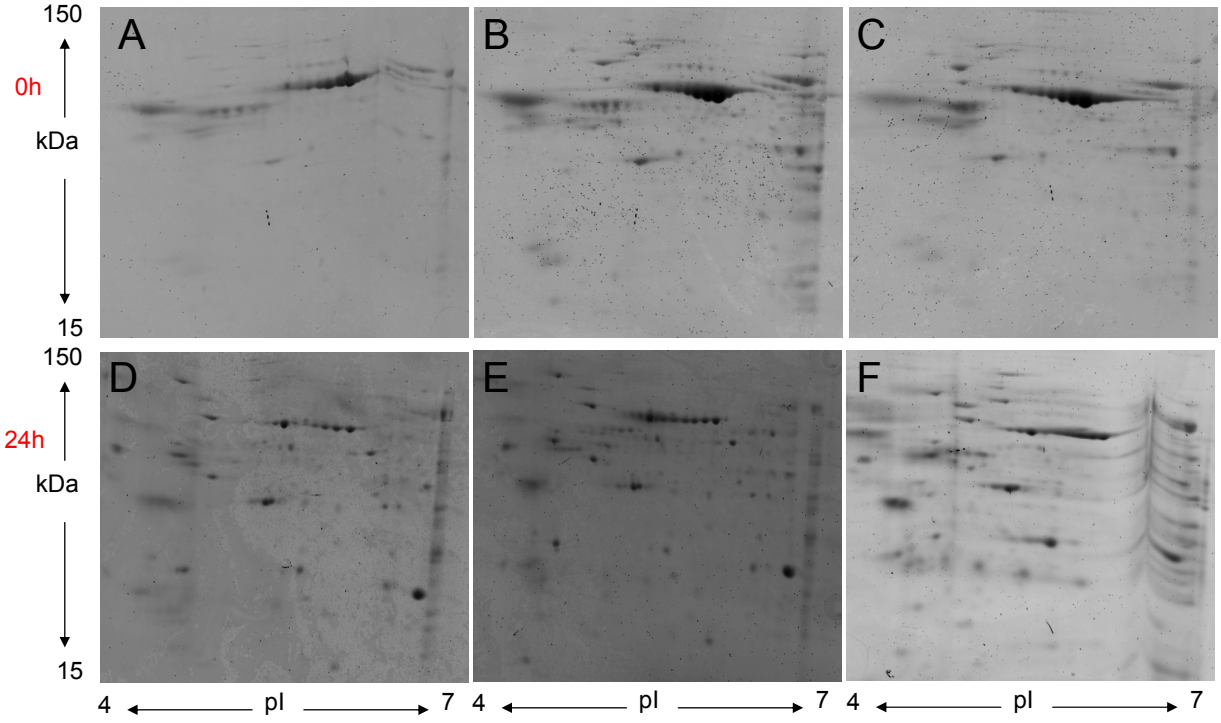

Figure S7: **2D-GE replicates of the B16F0 secretome.** Three gel replicates are shown for the 0 hour final wash (0 h secretome - Panels A-C) and 24 hour secretome (Panels D-F). Medium conditioned by B16F0 cells was concentrated and resolved in the first dimension on IPG strip 4-7 pH, 7cm. The second dimension is a 12% SDS-PAGE spanning molecular weight region 15-150kDa, stained with Coomassie blue and scanned using Typhoon 9400 scanner.

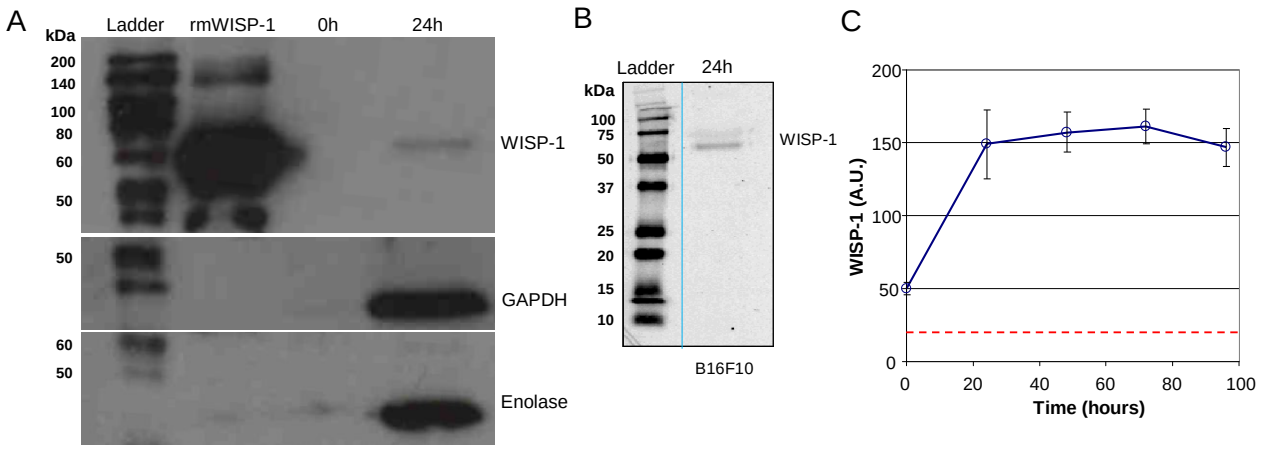

Figure S8: **Validation of the peptide mass fingerprinting and functional enrichment.** (A) Western blot was used to validate the expression of WISP-1 and alpha-enolase in B16F0-conditioned media as identified using proteomic workflow (Lane 1: Molecular weight ladder, Lane 2: recombinant mouse WISP-1, Lane 3: 0 hour background, and Lane 4: 24 hour secretome). GAPDH was used to support the functional enrichment of the exosomes within the set of secretome proteins. Membrane was probed for WISP-1, stripped and probed for GAPDH, and restripped and probed for alpha-enolase. Results representative of three replicates. (B) WISP-1 was detected by western blot in serum-free media conditioned for 24 hours by B16F10 cells. Under reducing conditions, the effective molecular weight is 65 kDa. Results representative of three replicates. (C) Accumulation of WISP-1 in B16F0-conditioned media was detected by ELISA (mean ± standard deviation, n=6). Dotted red line indicates detection threshold. Results shown for three technical replicates obtained for each of two biological replicates.

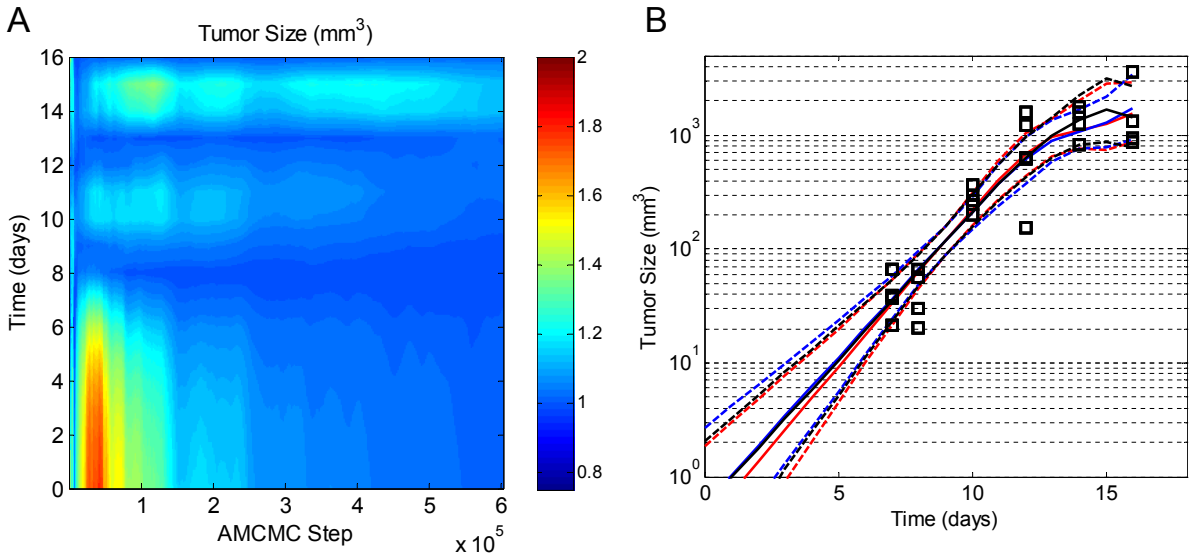

Figure S9: **Convergence of and posterior distributions in the Tumor Growth Model predictions.** (Panel A) A contour plot of the Gelman-Rubin statistic (i.e., the z-axis equals the potential scale reduction factor) of the model predictions as a function of time (i.e., the y-axis) calculated as a function of the cumulative chain up to a specific AMCMC step (i.e., the x-axis). Three parallel chains were used to calculate the Gelman-Rubin statistics for the model-based inference of the tumor growth. Values less than 1.2 suggest convergence of the chains. (Panel B) Comparison of the posterior distribution in the model predictions (lines) with the tumor growth data (squares). The most likely predictions are represented by the solid lines. The dashed lines enclose the 95% confidence intervals. The results from the converged segments of three different Markov chains, with 4.5×10^5 steps in each chain, are shown in different colors: chain 1 - blue, chain 2 - black, and chain 3 - red.

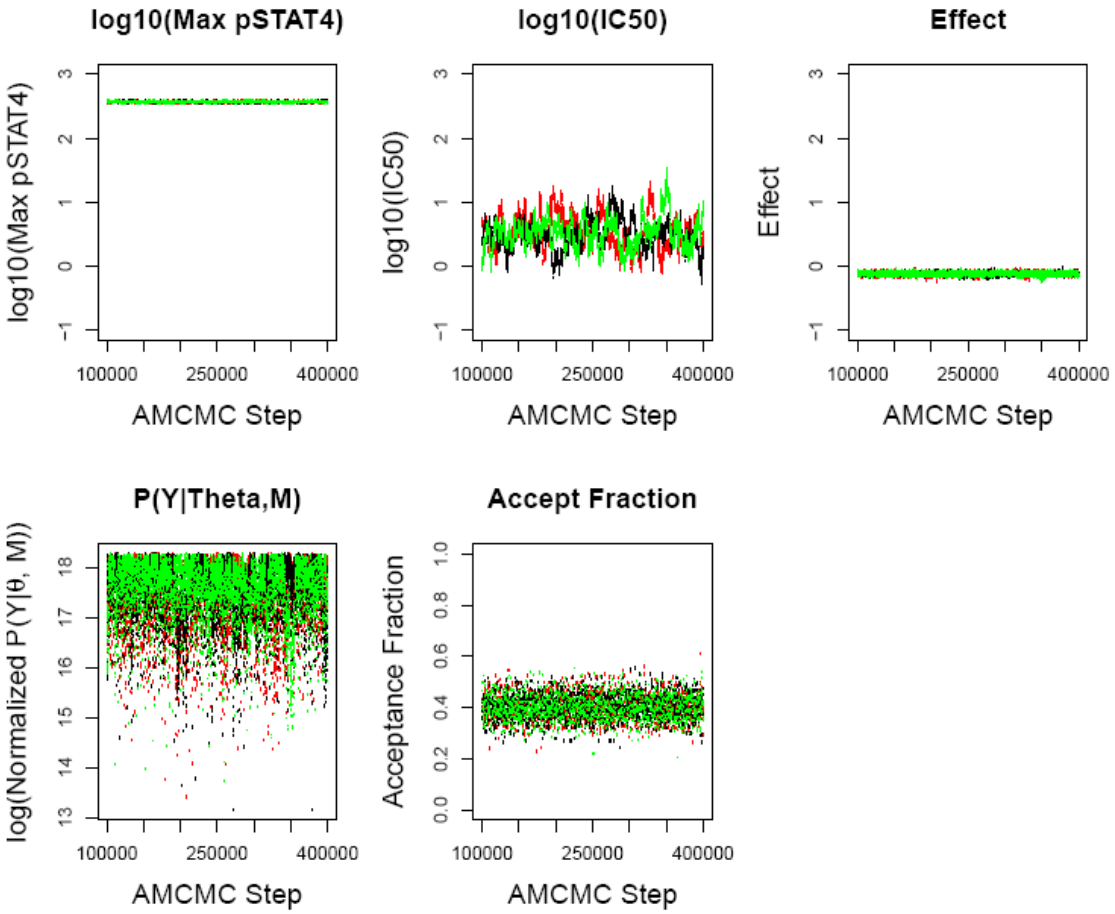

Figure S10: **Quantifying the inhibition of pSTAT4 by rmWISP-1 using an empirical Bayesian approach.** The trace of each of the model parameters (Max, $IC50$ and $Effect$), the likelihood evaluation ($P(Y|\Theta_{step}, M)$), and the AMCMC acceptance fraction are shown as a function of AMCMC step. The traces for three parallel chains are shown in different colors: Chain 1 (Blue), Chain 2 (Black), and Chain 3 (Red).

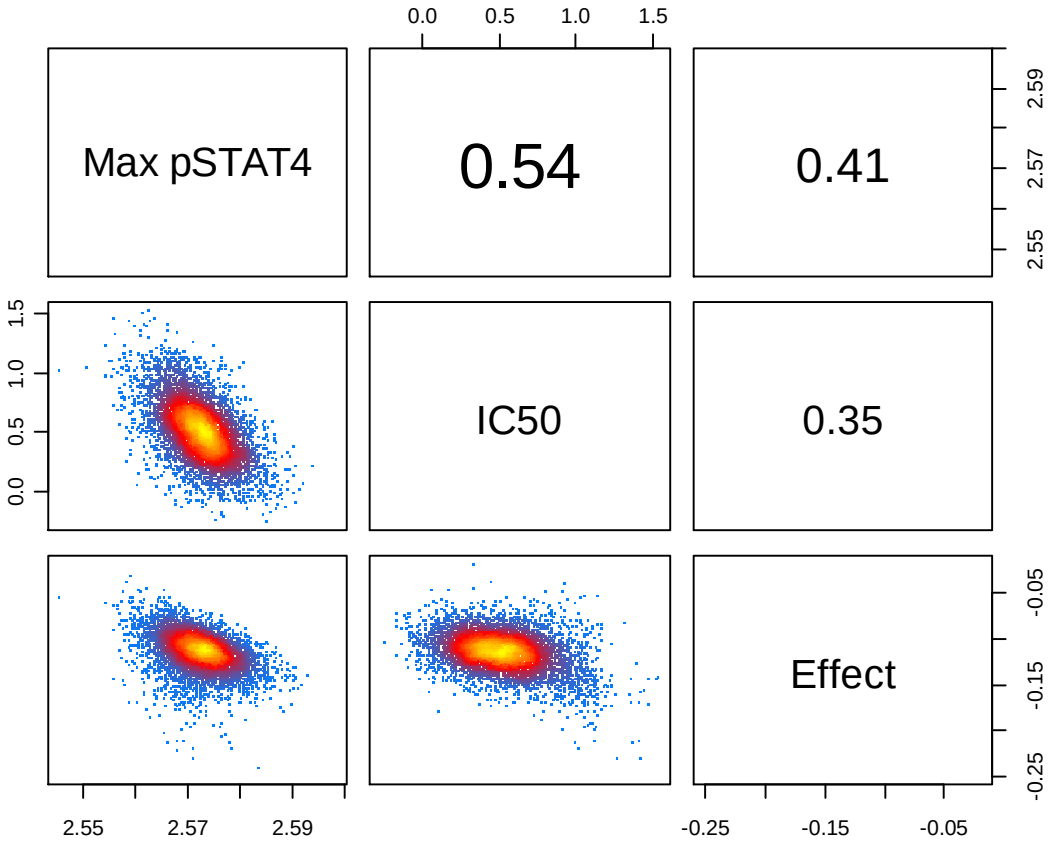

Figure S11: **Pairwise comparison of posterior distribution in rmWISP-1 inhibition parameters.** Parameter names are given on the diagonal. The log base 10 values of the $MaxpSTAT4$ and $IC50$ parameter are shown. Above the diagonal are the pairwise correlation coefficients of the parameters obtained from the three thinned Markov chains. Pairwise projections of the marginalized probability density are given below the diagonal. Coloring is based upon the estimated 2-D posterior density distributions using kernel density estimation.

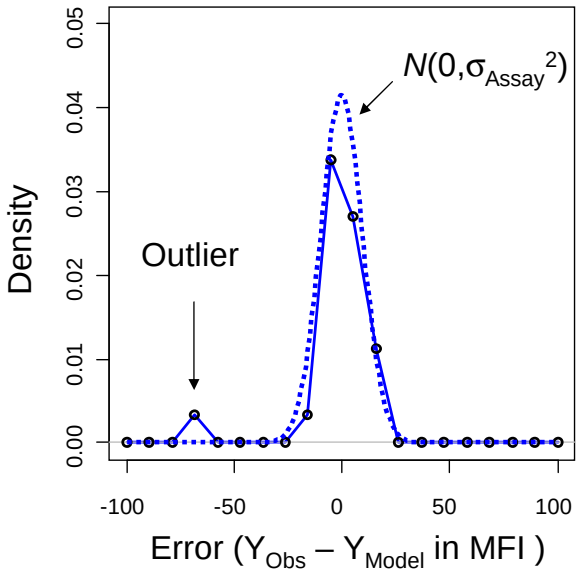

Figure S12: **Error analysis of inhibition of STAT4 activation by rmWISP-1.** An analysis of the error was used to identify an outlier in the rmWISP-1 data set. A gaussian distribution (dotted line - $N(0, 9.6^2)$) was compared against the histogram (circles) of the difference between observed (Y_{obs}) and predicted (Y_{Model}) STAT4 activation across all concentrations of rmWISP-1. The model predictions were obtained using the maximum likelihood parameter values.

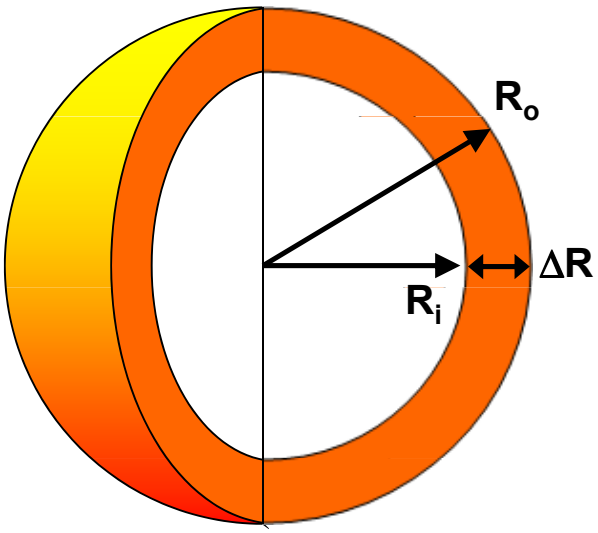

Figure S13: **Tumor spheroid model for WISP-1 expression.** The different models for WISP-1 expression were based upon a spherical tumor model where the tumor mass with an outer radius of R_o can be stratified into two different regions: 1) an actively proliferating zone (orange) between R_o and R_i and 2) an inner senescent/necrotic zone (white) with radius R_i.

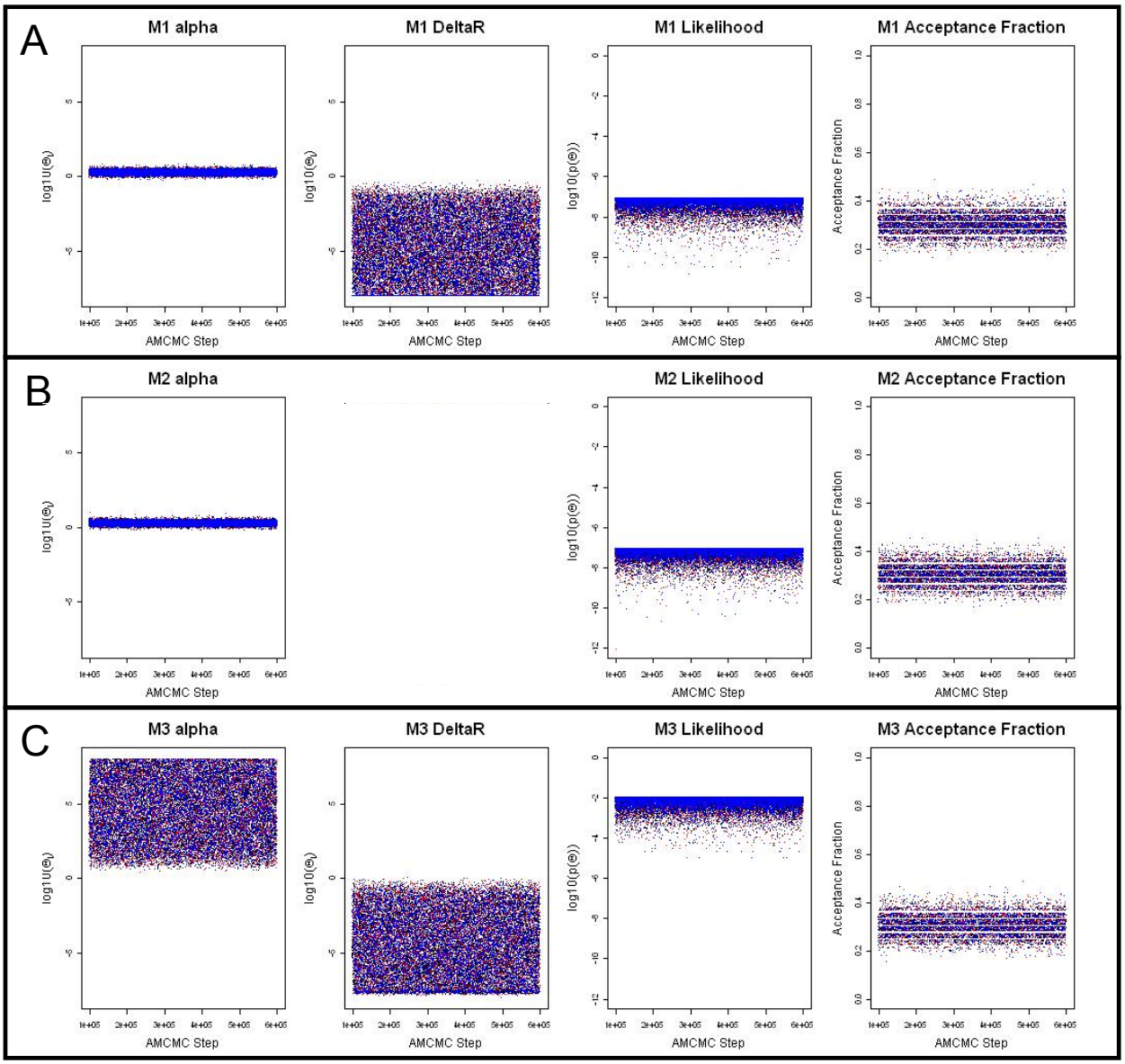

Figure S14: **Adaptive Markov Chain Monte Carlo integration of $P(M_i|Y)$ for WISP-1 expression models.** Results for each model are shown separately (Panel A: Model 1, Panel B: Model 2, and Panel C: Model 3). The trace of each of the model parameters (α and $DeltaR$), the likelihood evaluation ($P(Y|\Theta_{step}, M)$), and the AMCMC acceptance fraction are shown as a function of AMCMC step. The traces for three parallel chains are shown in different colors: Chain 1 (Blue), Chain 2 (Black), and Chain 3 (Red).

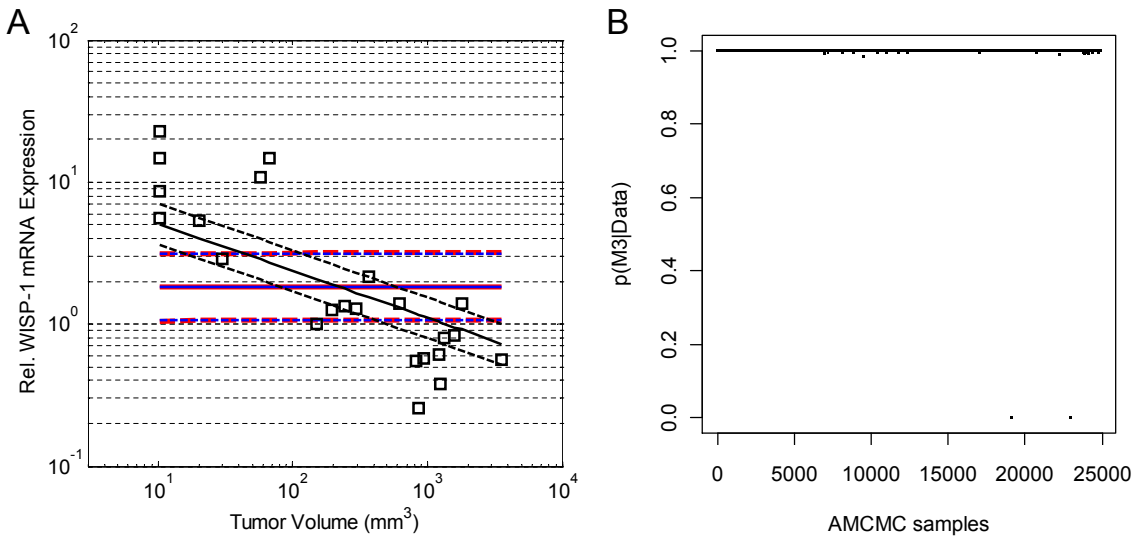

Figure S15: **Posterior predictions for competing WISP-1 expression models.** (Panel A) Comparison of the posterior distribution in the model predictions (lines) with the relative WISP-1 mRNA expression data (squares). The posterior distribution in results for each model are shown in different colors: Model 1 - blue, Model 2 - red, and Model 3 - black. The most likely predictions are represented by the solid lines. The dashed lines enclose the 95% confidence intervals. The posterior distributions reflect the collective results from the converged segments of three different Markov chains, with 5×10^5 steps in each chain. (Panel B) Evaluation of $P(M_3|Y)$ using the collective AMCMC results for $P(M_i|Y)$.